ELSEVIER

Chemical Physics 257 (2000) 235–252

Chemical Physics

www.elsevier.nl/locate/chemphys

Generalized oscillator strengths for inner-shell excitation of SF_6 recorded with a high-performance electron energy loss spectrometer

I.G. Eustatiu [a], J.T. Francis [b], T. Tyliszczak [b], C.C. Turci [c], A.L.D. Kilcoyne [d], A.P. Hitchcock [b,*]

[a] *Department of Physics and Astronomy, McMaster University, Ont., Canada L8S 4M1*
[b] *Department of Chemistry, McMaster University, Hamilton, Ont., Canada L8S 4M1*
[c] *Instituto de Química, Universidade Federal do Rio de Janeiro, 21910-900 Rio de Janeiro, Brazil*
[d] *Department of Physics, North Carolina State University, Raleigh, NC, USA*

Received 4 March 2000

Abstract

The generalized oscillator strength profiles for S 2p, S 2s and F 1s excited and ionized states of sulfur hexafluoride (SF_6) are reported up to very high momentum transfer. These have been measured with a variable impact energy, variable scattering angle electron energy loss spectrometer, which is dedicated to studies of electric dipole (optically allowed) and non-dipole (optically forbidden electric quadrupole and spin-exchange) inner shell electronic transitions of gases, and systematic measurements of their angular and impact energy distributions in order to derive generalized oscillator strength profiles. In addition to presenting the SF_6 results, we describe the design, construction and performance of the instrument, as well as data acquisition and analysis procedures.

1. Introduction

Absolute cross-sections (oscillator strengths) for both valence and inner shell excitation of atoms and molecules are required to understand high energy phenomena in a wide variety of fields including atmospheric chemistry, astrophysics, laser development, lithography and radiation physics. For example, dipole and non-dipole electronic spectroscopy of chlorofluorcarbons [1] is of great interest due to the participation of these species in the depletion of the ozone layer. The rarefied density of the stratosphere, combined with the presence of energetic particles mean that the formation and decay of states that are not dipole-coupled to the ground state, and also inner shell excited states, may play a role. These conditions are even more commonly met in the interstellar medium. Electron impact techniques, particularly electron energy loss spectroscopy (EELS) under variable momentum transfer conditions [2–4], have the capability of providing the required absolute cross-section information. The theoretical framework for describing dipole and non-dipole EELS

* Corresponding author. Fax: +1-905-521-2773.
E-mail address: aph@mcmaster.ca (A.P. Hitchcock).

0301-0104/00/$ - see front matter
PII: S0301-0104(00)00145-2

results within the first-Born approximation has been derived by Bethe [5] and elaborated in detail by Inokuti [6]. Non-dipole transitions have been studied using angle-resolved EELS in the valence-shell excitation of many species such as N_2 [7], O_2, CO, NO, CO_2, N_2O [8] and C_2H_2 [9] as well as in the inner-shell excitation of N_2, NO, N_2O [10], CO_2 [11,12] and sulfur hexafluoride (SF_6) [13–15].

In EELS, a mono-energetic beam of electrons of incident energy E_0 is elastically and inelastically scattered in single collisions with an atom or molecule in a field-free region. The energy and angular distribution of the inelastically scattered electrons gives detailed spectroscopic information about the excited states of the target. The basic electron energy loss process can be represented as

$$e^-(E_0) + M \rightarrow M^*(E_n) + e^-(E_1), \tag{1}$$

where e^- is the colliding electron with incident energy E_0 and residual energy (E_1) after a collision with the target species M that excites a transition from the ground state to an excited state of energy E_n. By energy conservation, in single scattering conditions $E_n = E_0 - E_1$.

Momentum is also conserved:

$$K = k_0 - k_1, \tag{2a}$$

$$K^2 = |K|^2 = |k_0 - k_1|^2 = k_0^2 + k_1^2 - 2k_0k_1\cos\theta, \tag{2b}$$

where k_0 is the wave vector of the incident electron with momentum $|k_0|$; k_1, the wave vector of the outgoing electron scattered through an angle θ with momentum $|k_1|$, and K, the resultant momentum transfer.

The states detected by single photon photoabsorption are limited by electric dipole selection rules. In contrast, EELS can provide a more complete investigation of atomic and molecular electronic structure, due to excitation of higher-order electric multipole transitions under conditions of significant momentum transfer, and excitation of spin forbidden electronic transitions under low energy impact. When the incident electron is highly energetic (large E_0) and is scattered through a small angle, the momentum transferred to the target from the colliding electron is very small, the interaction between this electron and the target is weak, and electric dipole processes dominate. When the scattering angle becomes large ($>10°$), the momentum transferred to the target from the incident electron during the collision increases which results in relaxation of the electric-dipole selection rules.

$f(K)$, the generalized oscillator strength (GOS) for electron scattering [5,6], which is defined as the intensity of a particular electronic transition at a specified momentum transfer, provides a very useful framework for quantitative analysis of inelastic electron scattering. The momentum transfer dependence of the GOS, which we call the GOS profile, can help determine the type of transition, thus aiding spectral assignment. In its range of validity (where the first Born approximation holds), the GOS concept condenses the (E_0, θ) variables into a single variable, K^2 (usually expressed in a.u.$^{-2}$). The GOS is related to the angular dependent differential cross-section for inelastic electron scattering by [5,6]

$$f(K) = (E_nk_0K^2/2k_1)(d\sigma/d\Omega), \tag{3}$$

where $d\theta/d\Omega$ is the measured differential scattering cross-section, which is the intensity of inelastic scattering of an incident beam of energy E_0 into a solid angle $d\Omega$ at a specific energy loss, E_n (for continuum processes, the relevant terms are $df(K)/dE$ and $(d^2\sigma/d\Omega\,dE)$). We note that, even outside the range of validity of the first Born approximation, one can express angular dependence of inner-shell intensities through an apparent GOS, since the more correct, angular dependent differential cross-section, can be readily derived as long as the impact energy is specified.

This paper describes the design, construction and operating procedures of an electron energy-loss spectrometer optimized for inner-shell spectroscopic studies under a wide range of experimental scattering conditions. The spectrometer performs quantitative studies of dipole allowed (small angle), spin forbidden (variable E_0), and dipole forbidden (variable angle), valence and inner-shell experiments. Other EELS spectrometers for inner-shell studies are optimized for only

one or a few of these areas. The Waterloo system [1,15–20] uses a fixed, high impact energy (2.5 keV), has a comparatively limited angular range, and modest energy resolution (0.8 eV FWHM). The Indiana [7] and Rome spectrometers [10] have a large angular range but modest resolution (>0.5 eV FWHM). The Manchester spectrometer [21,22] works at extremely low impact energies with modest resolution (~0.8 eV FWHM) and a fixed 90° scattering geometry.

The McMaster spectrometer has already been used to study non-dipole inner-shell excitation of a variety of species. Spin-forbidden, C 1s core excited triplet states of CO, C_2H_4, C_2H_2 and C_6H_6 have been characterized [23]. The momentum transfer dependence and vibrational structure of the (C $1s^{-1}$,π^*) $^3\Pi$ state of CO was investigated [24]. The spectroscopy and GOS profiles for S 2p and S 2s excitation of SF_6 [13,14,25,26] and for C 1s and O 1s excitation of CO_2 [11] have also been studied.

Good electron spectroscopy instrumentation [2–4] relies on a proper understanding of the optical properties [27] and practical realization of electron optical elements, such as lenses and dispersion elements [27–32]. An important concept is that of conservation of étendue, as expressed in the Helmholtz–Lagrange law. This requires compromises between beam current and energy resolution which are fundamentally related to the source brightness. In addition, at low electron energies space charge builds up and degrades the performance, particularly of electron monochromators [29]. The focusing and energy dispersing properties of hemispherical deflectors were first investigated by Purcell [30]. Later, Read et al. [31] concluded that hemispherical optics provide the best current-resolution compromise as monochromator and thus our spectrometer uses hemispherical optics for both monochromator and analyzer. The design principles used for the spectrometer are similar to those outlined in Ref. [32].

Our goal is to measure GOS profiles and systematically investigate their relationship to the electronic structure and bonding of the target species. The dependence of GOS values on electronic structure can be understood in further detail by recognizing that the GOS can be expanded as a power series in K^2 of terms involving the various electric multipole matrix elements [6] (Eq. (3)):

$$df/dE = A + BK^2 + CK^4 + \cdots, \tag{4}$$

where A is the optical oscillator strength (OOS):

$$A = \langle \varepsilon_1 \rangle^2, \tag{5a}$$

$$B = \langle \varepsilon_2 \rangle^2 - 2\varepsilon_1\varepsilon_3, \tag{5b}$$

$$C = \langle \varepsilon_3 \rangle^2 - 2\varepsilon_2\varepsilon_4 + 2\varepsilon_1\varepsilon_5, \tag{5c}$$

and ε_i is the ith order electric multipole matrix element ($i = 1$ dipole, 2 quadrupole, 3 octupole, etc.).

In the limit of zero momentum transfer (infinitely high energies and scattering angle of 0°), the GOS becomes the OOS. This cannot be measured directly by EELS since there is always a finite momentum transfer in every inelastic collision due to finite impact energy and finite scattering angles. However, a good estimate of the OOS can be derived in cases where the GOS is slowly varying at low K by extrapolating the measured GOS values to $K = 0$.

The modified Lassettre series [33,34], provides a semi-empirical connection between measured GOS profiles and the coefficients in Eqs. (5a)–(5c):

$$f(K,E) = \frac{1}{(1+x)^6} f_0 \sum_{n=0}^{m} \frac{f_n}{f_0} \left(\frac{x}{1+x} \right)^n, \tag{6}$$

where $x = K^2/[(2I)^{1/2} + (2|I - E_n|)^{1/2}]^2$, I is the ionization potential and E_n is the excitation energy of a particular discrete transition. Quantum mechanically, f_n are related to linear combinations of the respective multipole matrix elements. $f(0,E)$ is the OOS value.

The original Lassettre series was developed to quantitatively deduce precise OOS values by extrapolating GOS data measured by angle-resolved EELS, to the $K = 0$ limit. The second term in the series (f_1) is related to the quadrupole matrix element and the product of dipole and octupole matrix elements (Eq. (5b)) [2,35]. Higher-order terms give measures of other electric multipole contributions. In practice, the summation is usually limited to $m = 3$ since including higher-order

terms increases the error in lower terms, making their values unreliable. A direct electric quadrupole transition would be characterized by a positive f_1 value. In contrast, f_1 for an electric dipole transition is negative since the product of the dipole and octupole matrix elements is a larger positive value than the quadrupole matrix element. This results in a maximum for the quadrupole transitions and a continuous drop-off for the dipole transitions.

In order to demonstrate the spectrometer capabilities, this paper reports an extensive study of the GOS profiles for inner-shell excitation of SF_6. SF_6 is a very useful system to obtain a detailed understanding of inner shell excitation spectroscopy and core state dynamics. SF_6 belongs to a family of molecules in which a central atom forms polar bonds with two or more electronegative atoms as in BF_3, $SiCl_4$, etc. [36]. Nefedov [37] first proposed the existence of a potential barrier in molecules like SF_6. Initially, this barrier was attributed to a net repulsive interaction in the vicinity of the electronegative atoms in the molecule [36,37], but modern understanding [38–41] attributes the barrier to a centrifugal potential associated with high angular momentum of the ejected photoelectron since the continuum resonances appear at specific energies in selected angular-momentum partial waves of the outgoing electron in the final state.

The present work builds on recent GOS studies of SF_6 with the same spectrometer [11,13,14]. These studies of the GOS for S 2p and S 2s core excitation of SF_6 extend to much higher squared momentum transfer (up to $K^2 = 40$ a.u.$^{-2}$) than previous studies which had restricted the upper K^2 range to only 6 [15] or 18 a.u.$^{-2}$ [13]. This has allowed us to show definitively that the shapes of the GOS profiles for the two dipole forbidden bands (A,B) differ and that the B band must accommodate two or more states. Further, the GOS profiles for F 1s excitation of SF_6 are reported for the first time. All of the SF_6 results reported in this paper are new, having been obtained with a revised apparatus and different analysis procedures. Given that a major result of our earlier study [13] was a large disagreement (factors of 2–4) in the quantitative GOS values for inner shell excited SF_6 relative to those reported by Ying et al. [15], these new results are an important, independent test. We find very good agreement with our earlier results.

2. Spectrometer design

The spectrometer is a relatively conventional electrostatic-based design [2–4] which consists of a thermionic electron source, an optional monochromator, a collision region, an electron velocity analyzer, a detection system sensitive to single electrons (both serial and parallel detectors are used), along with several electrostatic lens systems to transport, accelerate, and condition the beam among these elements. Full hemispherical electrostatic deflectors are used for both monochromator and analyzer. Energy loss spectra, the distribution of electrons inelastically scattered by a sample gas at a fixed detection angle, are measured by retarding the electrons to a constant final energy (and therefore fixed resolution) prior to velocity analysis. The energy loss spectrum is scanned by adding the desired energy loss to the impact energy before the collision.

Our main goal is to study dipole-forbidden core excitation processes. Therefore, the electron optics has to accommodate impact energies from a few hundred eV to a few keV, the scattering angle has to be adjustable over a wide range (achieved in this case by mechanically scanning the analyzer and detector), and the overall efficiency of the optics and velocity selectors has to be as high as possible due to the low cross-sections of the features of interest.

Cross-sectional, three-dimensional and plan views of the spectrometer are presented in Fig. 1. The original design of the spectrometer is capable of variable impact energy (200–2000 eV) and variable scattering angle ($-35°$ to $+85°$), relative to the monochromator. Two pumping systems are used to provide differential pumping of the spectrometer relative to the gas sample, which is either an effusive jet or a collision cell. The deceleration lens, analyzer and detector are mounted on a computer controlled, rotatable platform. The *electron optics* were designed using principles enunciated by Kuyatt [42,43], tabulated lens

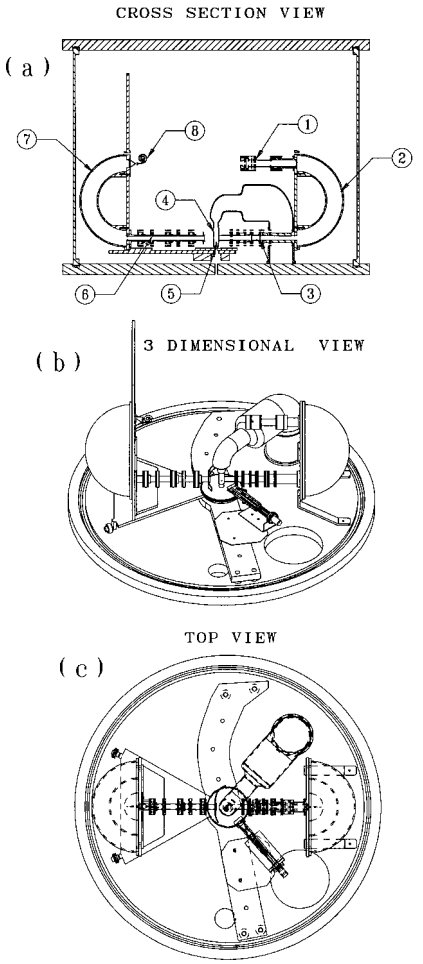

Fig. 1. Schematics of the spectrometer. (a) Cross-section view, showing (1) the electron gun, (2) the monochromator, (3) the monochromator exit lens, (4) the gas cell, (5) the capillary array, (6) the analyzer entrance lens, (7) the analyzer and (8) the detector. The (b) 3D view and (c) top view show both monochromated and unmonochromated implementations. The unmonochromated electron gun is positioned at the same level as the analyzer lens and faces the collision cell.

properties [27], and evaluated with the electrostatic lens design program SIMION [44], which analyzes charged particle trajectories in a system of electrostatic fields created by a collection of shaped electrodes, all tube type lenses of cylindrical symmetry in this case. The *electron gun* is a design adapted from Tronc (private communication), which produces high current at low electron energy. Thermionic emission from a DC-heated tungsten hairpin filament is used since it has better stability, higher emission, and reduced sensitivity to reactive gases, relative to indirectly heated oxide cathodes. The *monochromator exit lens*, a design adapted from a five-element lens of Heddle and Papadovassilakis [45], accelerates the energy selected beam of low energy electrons (typically 10–25 eV) up to the impact energy (200–2000 eV). The *analyzer entrance lens* accepts inelastically scattered electrons, decelerates and focuses them to the analyzer pass energy at the analyzer entrance plane. After exploring a number of less complex designs, a seven elements lens was selected. Fig. 2 characterizes the voltages ratios used for the monochromator and analyzer lenses. These ratios are derived from the experimental operational voltages, which are routinely recorded. Table 1

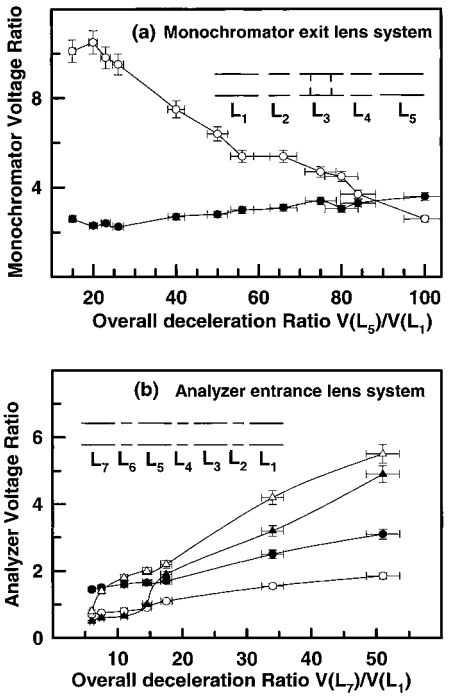

Fig. 2. (a) Characteristic lens voltage ratios as a function of the overall acceleration ratio $V(L_5)/V(L_1)$ for the monochromator exit lens (● – $V(L_4)/V(L_2)$; ○ – $V(L_3)/V(L_2)$); (b) Characteristic lens voltage ratios as a function of the overall deceleration ratio $V(L_7)/V(L_1)$ for the analyzer entrance lens (● – $V(L_5)/V(L_3)$; ○ – $V(L_3)/V(L_1)$; ▲ – $V(L_4)/V(L_2)$; △ – $V(L_6)/V(L_4)$). The inset figures are schematics of the monochromator exit lens and analyzer entrance lens.

Table 1
Theoretical vs. experimental voltage ratios for spectrometer lenses

Acceleration ratio $V(L_5)/V(L_1)$	$V(L_4)/V(L_2)$		$V(L_3)/V(L_2)$	
	Experiment	Theory	Experiment	Theory
Monochromator exit lens				
15	2.6	1.7	**10.1**[a]	**0.3**[a]
50	2.8	2.9	6.4	1.4
100	3.6	2.5	**2.6**[a]	**0.7**[a]

Deceleration ratio $V(L_7)/V(L_1)$	$V(L_4)/V(L_2)$		$V(L_6)/V(L_4)$		$V(L_5)/V(L_3)$		$V(L_3)/V(L_2)$	
	Experiment	Theory	Experiment	Theory	Experiment	Theory	Experiment	Theory
Analyzer entrance lens								
5	1.4	1.3	0.8	0.4	1.5	2.5	0.8	0.6
50	5.0	2.9	**5.6**[a]	**0.3**[a]	3.0	13.2	**1.8**[a]	**0.5**[a]

[a] Bold entries indicate lens operation on a different electron optical branch from that predicted theoretically (see text).

compares lens ratios predicted from the theoretical simulations with those observed in practice. While the voltages predicted by the SIMION [44] simulations provided useful starting points for initial operation of the spectrometer, over time, tuning (often through a multi-parameter computer optimization procedure) has lead to rather large deviations from the anticipated voltages. Examination of the focus curves in standard electron optics texts [27] indicates that any lens with three or more elements has at least two sets of conjugate object-image points. We believe the deviations between actual and predicted optimum voltage ratios represent a shift from one operating branch to another in the complex focus parameter space. The data in Table 1 should be useful for those evaluating the extent to which SIMION-based lens optimization procedures actually predict global, as opposed to local, optima. Both the monochromator and analyzer dispersion elements are full 180° hemispherical electrostatic deflectors since this geometry provides superior performance for electron scattering studies that are differential in both energy and angle [31,46].

The *collision region* can be configured in two ways. In the early period of operation, the gas was introduced as an effusive jet formed by expansion through a metallic capillary array. [1] For recent high momentum transfer studies, where intensity is critical, the capillary array was surrounded by a collision cell, to achieve a higher gas density without increasing the apparatus working pressure.

For all work published to date, the detector has been a channel electron multiplier. The amplified pulses from single electrons are processed using standard pulse counting techniques with a custom built combined pre-amplifier, amplifier and discriminator circuit. Recently a resistive anode, position sensitive parallel detector (Quantar 3300 [2]) has been installed and has been shown to provide a significant enhancement in signal rates over single channel detection [47]. The computer-controlled DC lens supply *electronics* were designed and constructed in-house.

In order to demonstrate the performance in the monochromated mode, Fig. 3(a) presents vibrationally resolved spectra of the (C $1s^{-1}$,π^*) $^3\Pi$ and (C $1s^{-1}$,π^*) $^1\Pi$ states in CO at 285.9 and 287.4 eV recorded with an energy resolution of 0.18 eV [25]. The dipole regime performance is inferior to that of the highest performance inner shell energy loss spectrometers [32,48–50], but the ability to achieve vibrational resolution under the low cross-section near threshold conditions needed for exciting the triplet state is rare. This capability allows us to study vibrational resolved non-dipole core excita-

[1] Minitubes – Grenoble, 7, Ave. de Grand Chatelet, 38100 Grenoble, France.

[2] Quantar Technology Inc., Santa Cruz, CA, 95060.

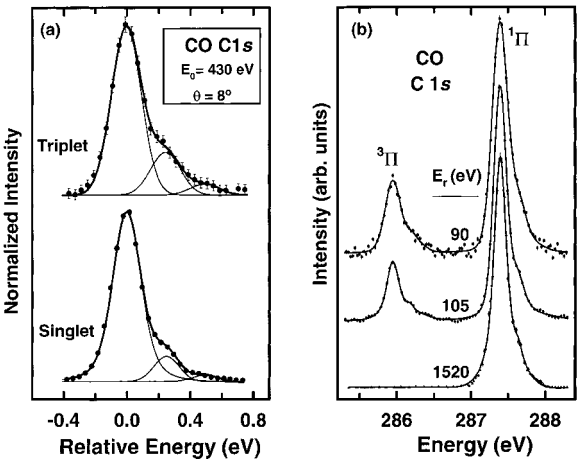

Fig. 3. (a) Vibrational band structure of the $X^1\Sigma^+ \rightarrow (C\ 1s^{-1}, \pi^*)^3\Pi$ and $X^1\Sigma^+ \rightarrow (C\ 1s^{-1}, \pi^*)^1\Pi$ transitions recorded at 1520 and 140 eV residual energy, 8° scattering angle and 0.18 eV FWHM resolution. The peaks have been placed on a relative energy scale to facilitate line shape comparison. (b) Electron energy loss spectra of CO in the region of the ($C\ 1s^{-1}$, π^*) $^3\Pi$ and $^1\Pi$ states recorded at residual energies of 90, 105 and 1520 eV and scattering angles of 4°, 4° and 2°, respectively [24].

tion in many systems. Fig. 3(b) demonstrates the variable impact energy capability of the spectrometer with results of a study of the ($C\ 1s^{-1}$,π^*) $^3\Pi$ state of CO at 286.0 eV, which is only detectable when the impact energy approaches the energy of excitation [24]. Inner-shell experiments at low impact energy are particularly difficult since both high resolution and high sensitivity are needed to detect these weak processes. Ref. [13] presents S 2p spectra of SF_6 recorded under conditions of quite different scattering angle and impact energy, but with nearly constant momentum transfer. This type of experiment, which exploits both the variable angle and variable impact energy capability of the spectrometer, is very useful to check for validity of the first-Born approximation [5,6] which is a fundamental underlying assumption of the GOS concept.

In order to provide greater signal at large momentum transfer, a configuration for unmonochromated operation was implemented. For this, a commercial, glancing incidence Auger electron gun is mounted beside the monochromator (Fig. 1). This electron gun provides an electron beam of much greater intensity (up to 10 μA vs. <0.1 μA in monochromated mode), an acceptable beam size (~1 mm), and modest energy resolution (0.6–0.8 eV). The beam is formed by tungsten filament emission, a standard anode-grid-focus combination, and a pair of deflector plates at the gun exit for beam steering. The beam goes through the gas cell and either hits the side of the analyzer entrance lens, or is trapped by a current monitoring plate at large scattering angles. The electron guns for monochromated and unmonochromated operation are powered by the same electronics. In order to have good differential pumping between the main chamber and the collision region, a collision cell was installed around the capillary array, thus greatly increasing the gas density in the scattering region and therefore the intensity of the inelastically scattered signal.

3. Operating procedures and data analysis

The GOS for a particular electronic transition as a function of momentum transfer (K) is called the GOS profile. GOS profiles are plotted in terms of K^2 rather than K since the Bethe-Born expansion (Eq. (4)) is expressed in even powers of K. In order to obtain an absolute GOS profile, all other factors, such as pressure, incident beam current, acquisition time, etc., that determine the signal strength, are either held constant, or variations in their values are measured and taken into account. Thus, the raw data is systematically normalized to beam current, gas pressure, and acquisition time. With appropriate normalization (and compensation for this normalization when error bars are being evaluated), spectra acquired under different conditions can be combined in order to provide better statistics. In addition to ensuring reliable and reproducible observations, it is necessary to correct for several systematic distortions, and to convert the measured relative cross-sections to absolute oscillator strengths. The measurements are made in one of two modes, called "energy-scan" and "angle-scan", each of which are described below, along with the procedures used to derive absolute GOS profiles.

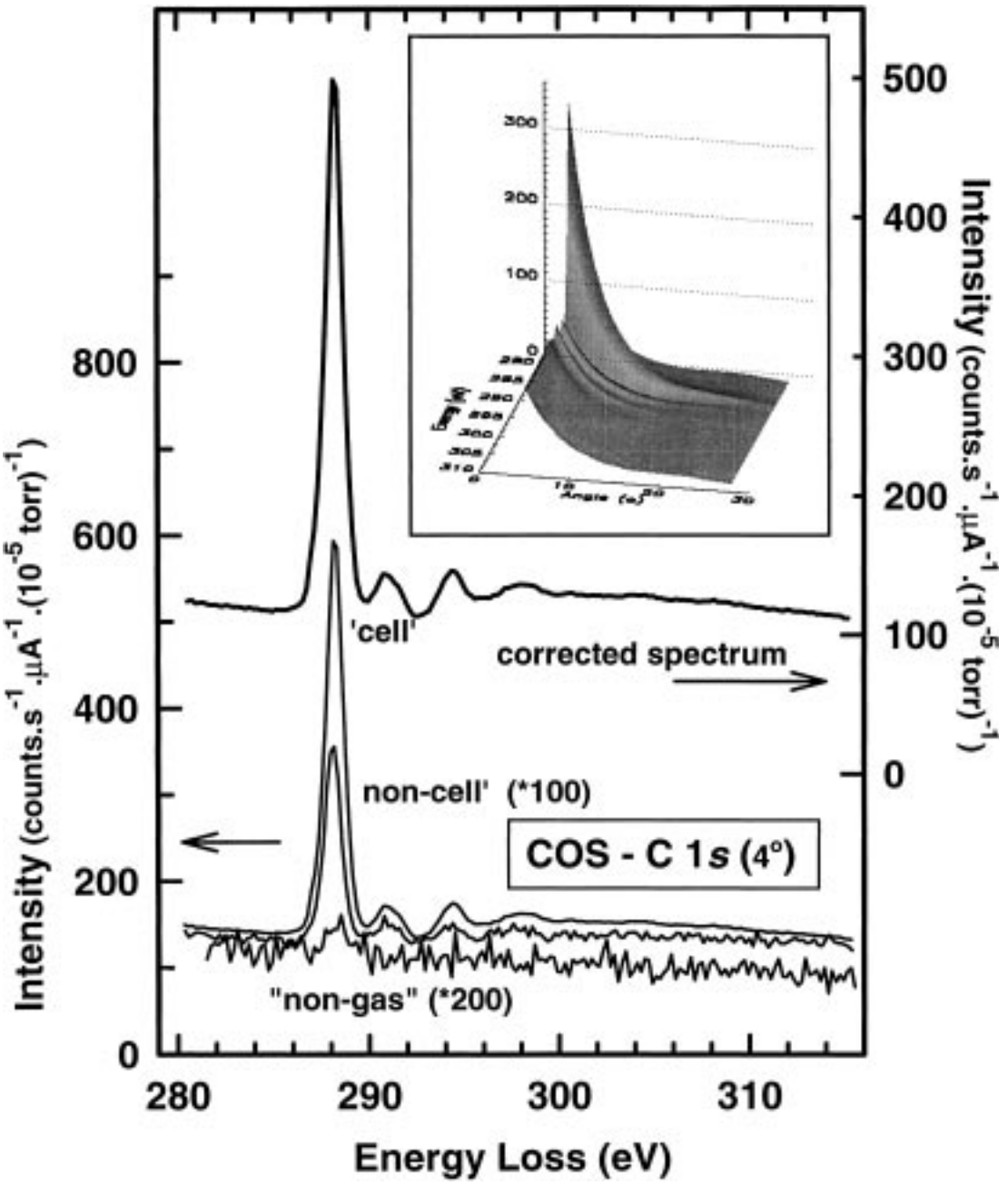

Fig. 4. Cell, non-cell and non-gas as-recorded spectra for C 1s excitation of COS measured at 4° with a final electron energy of 1300 eV. Each spectrum has been normalized to time, pressure and beam current. The inset figure shows the raw data from angle-scan measurements of the angular dependence of the C 1s excitation spectrum of COS.

3.1. Acquisition modes

3.1.1. Energy-scan mode

In the energy-scan mode, high quality signal-averaged energy loss spectra are recorded at a fixed scattering angle under conditions called "cell", "non-cell" and "non-gas". The cell mode is the conventional spectrum with high sample gas density in the collision cell. In the non-cell measurement, the sample is introduced outside of the collision cell to the same main chamber pressure. The non-cell spectra are acquired to subtract the signal from scattering by gas outside the collision cell. In the non-gas measurements, the signal from residual gas, detector background and scattering of the wings of the main beam from parts of the apparatus is measured. It is important to measure non-gas spectra regularly to check the spectrometer tuning. If the spectrometer is tuned correctly this signal is less than 1% of the cell signal. At each scattering angle, the cell spectra are subtracted from the non-cell spectra. The corrected spectrum used for subsequent processing is obtained from the difference (cell–non-cell), and normalized to the pressure in the collision cell during the cell measurements. This corrected spectrum contains only the contribution from the main gas density in the collision cell. Fig. 4 shows cell, non-cell and non-gas C 1s spectra of COS recorded at 4°, and a final electron energy of 1300 eV, along with the corrected spectrum. Energy scales are calibrated by recording the spectrum of a gas mixture, using the energy of a well-known transition as reference (e.g., the C 1s $\rightarrow \pi^*$ of CO_2 [50]).

Relative cross-sections for each resolved electronic transition are then derived. First, the underlying ionization continuum background is removed by subtracting a smooth curve determined from a curve fit of a linear, binomial or exponential function to the continuum structure below the onset of core excitation. The background subtracted spectra are then simultaneously fit using a multi-file optimization procedure [51] to a spectroscopic model consisting of a combination of Gaussian peak shapes and arc tangent or error function edge shapes to represent the ionization continua. The peak areas associated with each feature are geometry-distorted relative cross-sections. They are determined for each feature at all scattering angles at which energy-scan spectra are acquired.

Next, a geometric correction, $G(\theta)$ shown in Fig. 5, is applied to the measured relative cross-sections. This correction takes into account two factors: first, the changes in geometric overlap caused by changes in the size and shape of the interaction region with the scattering angle (the collision path length in high gas density regions is longer at small angles); second, the existence of a non-uniform gas distribution inside the collision cell. Brinkman and Trajmar [52] have presented a detailed discussion of the importance and methodology of these corrections for electron scattering from effusive jet gas sources. Here, we outline our approach for correction when the sample is a gas cell. There are several approximations involved.

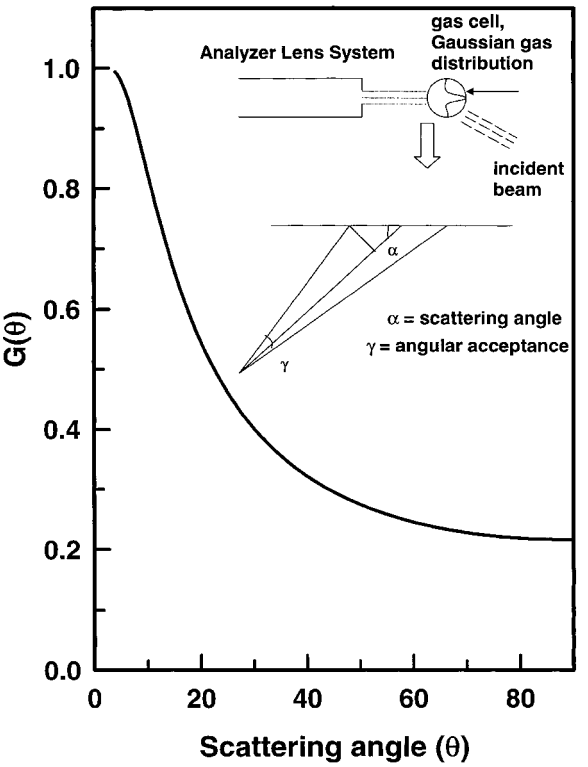

Fig. 5. Geometric correction function used to correct the angular dependence of the overlap of incident beam, analyzer viewing cone, and spatial variation of the gas density. The inset schematic shows the geometry used to derive the analytical form for the correction factor.

The entrance of the analyzer is assumed to be a point, the incident and scattered flux are assumed to be parallel beams; and the gas density in the cell is assumed to be a Gaussian distribution. The geometric correction as a function of the scattering angle is obtained by integration of the Gaussian function $f(z)$ that represents the gas distribution in the intersection volume and is expressed as

$$f(z) = A\exp[(-\ln 2^{*}z^{2})/(w/2)^{2}], \tag{7}$$

where A is the amplitude factor used to normalize the geometrical correction to a maximum value of 1 and z is half of the acceptance length of the beam, obtained from geometrical considerations (see Fig. 5 for definitions of the angles):

$$z = \mathrm{d}\tan\gamma/(\sin\theta + \cos\theta\tan\gamma). \tag{8}$$

This correction function is specific to our gas cell. Other corrections must be developed for different spectrometers. For example, the earlier GOS studies [13,25] used an effusive jet as the sample and thus required a very different geometric correction procedure. Other methods for correcting for finite scattering volume and detector geometry effects have been reported by Bonham [53,54].

3.1.2. Angle-scan mode

In the 'angle-scan' mode, the signal averaged measurements are carried out using scattering angle rather than energy loss as the control parameter. However, since the speed of mechanical scanning is limited, we optimize the acquisition process by measuring signals at a number of energy loss values at each scattering angle. An example of raw data from an angle-scan is given by the inset in Fig. 4. For a fixed acquisition period, the angle-scan mode provides a means of achieving a much denser sampling of the scattering angle (and thus momentum transfer), thereby providing more detailed GOS profiles. However, high quality energy-scan mode spectra are essential to ensure proper spectroscopic analysis at all momentum transfers, and to allow checks for systematic errors. If the spectrometer operates with the correct and stable tuning (i.e., there is no insulating contamination of the spectrometer surfaces or beam degradation over the period of the measurements), the normalized and calibrated 'angle-scan' and 'energy-scan' data recorded for the same energy loss range, the same K^2, and same impact energy, are the same within mutual experimental uncertainties. This is often, but not always, the case. Comparison of angle-scan and energy-scan results is carried out to detect systematic errors in either mode.

The 'angle-scan' data is analyzed using the same multi-file fitting procedure described in the energy-scan mode. After an acceptable multi-file fit for all energy-scan spectra, the angle-scan spectra are added and the fit is repeated, such that the final result is determined by a unified treatment of the energy-scan and angle-scan data. It is critical to have accurate energy calibration of all spectra, since the energy positions and the peak widths are kept constant in the multi-file fitting procedure. After determining the peak areas, the geometric and the kinematic corrections are applied to the angle-scan results, just as in the energy-scan analysis, to obtain relative GOS.

3.2. Absolute generalized oscillator strengths

The limiting behavior at small K values can be used to normalize the relative GOS to previously determined absolute OOS, the GOS at $K = 0$. Typically, the GOS is extrapolated over a range of low K^2 values to $K^2 = 0$ to obtain $f_{\mathrm{rel}}(0)$. The ratio of $f_{\mathrm{rel}}(0)$ to the OOS for one or more strong transitions provides a scale factor which is used to convert all of the relative GOS to absolute GOS profiles. The extrapolation may be done by a number of methods [53–55]. Section 4 illustrates the results obtained for SF_6.

Experimental uncertainties for the derived GOS values are typically determined from the energy-scan data. The uncertainty is the quadrature sum of the uncertainties in the momentum transfer (K^2) and in the peak area determination. The uncertainty in K^2 is determined from propagating the uncertainty in the scattering angle (0.25°) through to the associated K^2 value (Eq. (2b)). The uncertainty in the peak area includes uncertainty in the gas pressure (~2%) and the incident beam current (~1%), along with contributions from the statistical precision of the data, all added in quadrature.

It should be noted that significant systematic errors may be associated with various aspects of the data treatment. A proper geometric correction is important [52] since, if the geometrical correction is not applied the intensity of the signal at low scattering angles is substantially overestimated. Finally, the absolute GOS values are only as accurate as the literature OOS to which we normalize our relative values. The spread in literature OOS values can be as high as 30%.

4. Generalized oscillator strengths for inner shell excitation of SF_6

In order to illustrate the instrumental performance for measuring absolute GOS over wide momentum transfer ranges, we present detailed results for the S 2p, S 2s and F 1s GOS profiles of SF_6. The scientific motivation for this study, and its relationship to earlier studies are given in Section 1 of this paper. Ref. [25] discusses the inner shell spectroscopy of SF_6 in detail while Ref. [26] presented the S 2p and S 2s spectra at very high momentum transfer.

4.1. SF_6 inner shell spectroscopy

Fig. 6 compares energy loss spectra of SF_6 at the S 2p, S 2s and F 1s edges, recorded under dipole-dominated and non-dipole conditions. Tables 2–4 list the peak energies used in the data analysis, along with their spectral interpretation [25,56].

The dipole-regime S 2p spectrum is dominated by three bands, corresponding to excitation to the dipole coupled states arising from S 2p excitation

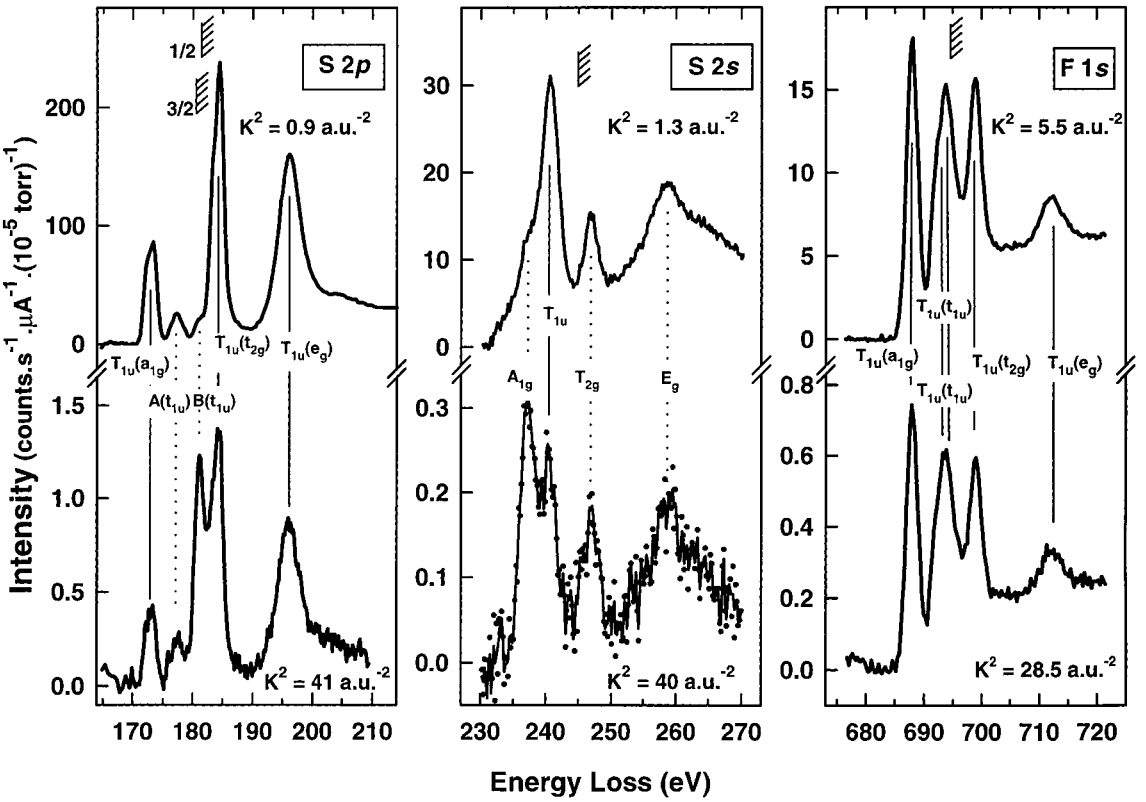

Fig. 6. Background subtracted electron energy loss spectra of SF_6 recorded with 1400 eV final electron energy in the S 2p, S 2s and F 1s region in both near-dipole (4°) and non-dipole conditions (F 1s – 24°, S 2s – 36°, S 2p – 36°). The hatched lines indicate the ionization potentials as measured by photoelectron spectroscopy [60,61].

Table 2
Energies, widths, line shapes and optical oscillator strengths derived from a constrained multiple file curve-fit analysis of the S 2p spectra of SF_6

State	E (eV)[a]	Line type	Width (eV)[a]	OOS ($\times 10^{-2}$)[b]			
				This work	Literature		
					[13]	[36]	[56]
$T_{1u}(a_{1g})$-3/2	172.5	Gaussian	1.41	9.1	7.9	9.6	8.7
$T_{1u}(a_{1g})$-1/2	173.6	Gaussian	1.14				
$A(t_{1u})$	177.5	Gaussian	2.86	3.5	0.9		
Continuum 1[c]	180.4	Error function	1.50				
IP (3/2)[d]	180.4						
IP (1/2)[d]	181.6						
$B(t_{1u})$	181.2	Gaussian	2.06	0.06	0.06		
$T_{1u}(t_{2g})$-3/2	183.4	Gaussian	1.10	21	23	23	18
$T_{1u}(t_{2g})$-1/2	184.6	Gaussian	1.06				
Continuum 2[c]	192.8	Error function	2.50				
$T_{1u}(e_g)$	195.9	Gaussian	2.73	19	20	34	24
$T_{1u}(e_g)$	197.4	Gaussian	3.36				

[a] The energy and width of each feature is fixed to these values during the fit. Only the intensities were varied in fitting the spectrum at each angle.
[b] The GOS scales were set by normalizing the extrapolated OOS for the sum of the 3/2 and 1/2 components of the values reported by Dehmer [36] (0.096 for a_{1g} and 0.23 for t_{2g}) and by Blechschmidt et al. [58] (0.087 for a_{1g} and 0.18 for t_{2g}). In the fitting, the 3/2 and 1/2 components were fit separately.
[c] The spectra are fit to two separate continua to take into account inner-well and outer-well regions of the potential barrier. The details are discussed in Ref. [13].
[d] Ionization potential from XPS measurements [60,61].

Table 3
Energies, widths, line shapes and optical oscillator strengths derived from a constrained multiple file curve-fit analysis of the S 2s spectra of SF_6

State	E (eV)[a]	Line type	Width (eV)[a]	OOS ($\times 10^{-2}$)[b]
$A_{1g}(a_{1g})$	237.4	Gaussian	2.83	1.5
$T_{1u}(t_{1u})$	240.4	Gaussian	2.83	3.6
Continuum	244.7	Arctangent	1.25	
IP[c]	244.7			
$T_{2g}(t_{2g})$	246.8	Gaussian	2.14	0.7
$E_g(e_g)$	258.5	Gaussian	5.10	1.3
$E_g(e_g)$	262.8	Gaussian	7.97	

[a] The energy and width of each feature is fixed to these values during the fit. Only the intensities were varied in fitting the spectrum at each angle.
[b] GOS scale set by correlating S 2s and S 2p scales in a simultaneous measurement of both edges under near-dipole conditions.
[c] Ionization potential from XPS [61].

to the a_{1g}, t_{2g} and e_g virtual valence orbitals. Under strong non-dipole conditions, there are two additional bands (A and B) which are associated with non-dipole coupled states arising from S 2p excitation to the t_{1u} virtual valence orbital. At strongly non-dipole conditions, the relative intensity of the second dipole forbidden feature increases dramatically to the extent that, above $K^2 \sim 40$ a.u.$^{-2}$, the transition to the "B state" becomes the most intense spectral feature, even stronger than the transition to the $T_{1u}(t_{2g})$ state which dominates the dipole spectrum [26].

Because the S 2s core level has opposite parity to the S 2p level, the dipole/non-dipole character

Table 4
Energies, widths, line shapes and optical oscillator strengths derived from a constrained multiple file curve-fit analysis of the F 1s spectra of SF_6

State	E (eV)[a]	Line type	Width (eV)[a]	OOS ($\times 10^{-2}$)[b]
$T_{1u}(a_{1g})$	687.9	Gaussian	2.36	10.7
$T_{1u}(t_{1u})$	691.4 (sh)	Gaussian	1.66	2.1
$T_{1u}(t_{1u})$	693.5	Gaussian	3.25	17.6
Continuum	694.6	Error function	1.3	
IP[c]	694.6			
$T_{1u}(t_{2g})$	698.8	Gaussian	2.60	9.9
$T_{1u}(e_g)$	712.1	Gaussian	4.41	4.7

[a] The energy and width of each feature is fixed to these values during the fit. Only the intensities were varied in fitting the spectrum at each angle.
[b] GOS scale was set by matching the relative data to the absolute GOS value at $K^2 \sim 4$ a.u.$^{-2}$ [25].
[c] Ionization potential from XPS [61].

of transitions to the same upper level is reversed. In addition, since the S 2s level is non-degenerate, the orbital and state picture of the S 2s spectroscopy are interchangeable, which is not the case for the S 2p or F 1s excitation, where a full state picture is essential [25]. Thus, there is only one dipole-allowed S 2s excitation and three dipole-forbidden, quadrupole-allowed S 2s transitions. As shown in Fig. 6, there is a very marked rearrangement of spectral intensities with increasing momentum transfer, as discussed earlier [26].

A correct symmetry analysis of F 1s excitation of SF_6 [25] shows there are five excited states that are dipole coupled to the ground state. A superficial examination of the F 1s spectrum suggests that there are four resonances corresponding to F 1s excitations, which previously had been assigned to the four virtual valence orbitals [57]. A closer examination reveals a distinct shoulder on the second peak, with an energy of 692.4 eV, which is 1.6 eV below the peak maximum at 694.0 eV. The F 1s spectral shape changes negligibly with increasing momentum transfer, suggesting that either the dipole states dominate at all scattering conditions or that any additional quadrupole states are not energy resolved and have similar GOS profiles such that their contributions are merged with the apparent dipole contributions. Interestingly, a recent combined experimental–computational study of the GOS for O 1s excitation of CO_2 [11] suggested that in cases of core excitation from chemically equivalent sites, the non-dipole excitation channel can be as strong as the dipole channel at finite momentum transfer.

4.2. GOS profiles for inner shell excitation of SF_6

4.2.1. S 2p

Generalized oscillator strength profiles are shown for three dipole allowed S 2p transitions and for the S 2p continuum in Fig. 7, and for the two dipole-forbidden S 2p transitions in Fig. 8. The absolute GOS scale for the S 2p region was set by matching the graphical extrapolation to $K^2 = 0$ of the relative GOS profile for the $T_{1u}(a_{1g})$ and $T_{1u}(t_{2g})$ states to the average values reported by Dehmer [35] (0.096 for a_{1g} and 0.23 for t_{2g}) and by Blechschmidt et al. [58] (0.087 for a_{1g} and 0.18 for t_{2g}). Since there is significant disagreement in the literature OOS values, using the mean literature OOS implies ~15% uncertainty in the absolute GOS values. The results derived from the 'energy-scan' and 'angle-scan' modes are plotted separately. In almost all cases, there is good agreement between these two sets of results. Fits of the GOS profiles to a three-term, modified Lassettre series (Eq. (6)) are also plotted in Figs. 7 and 8 (and the other figures reporting GOS). The coefficients from the Lassettre fits are summarized in Table 5.

The GOS for all three dipole-allowed transitions decay relatively smoothly to higher K^2 from a maximum at $K^2 = 0$. The shape and absolute values determined in this work are in good agreement with our previous results [13]. The spectrometer

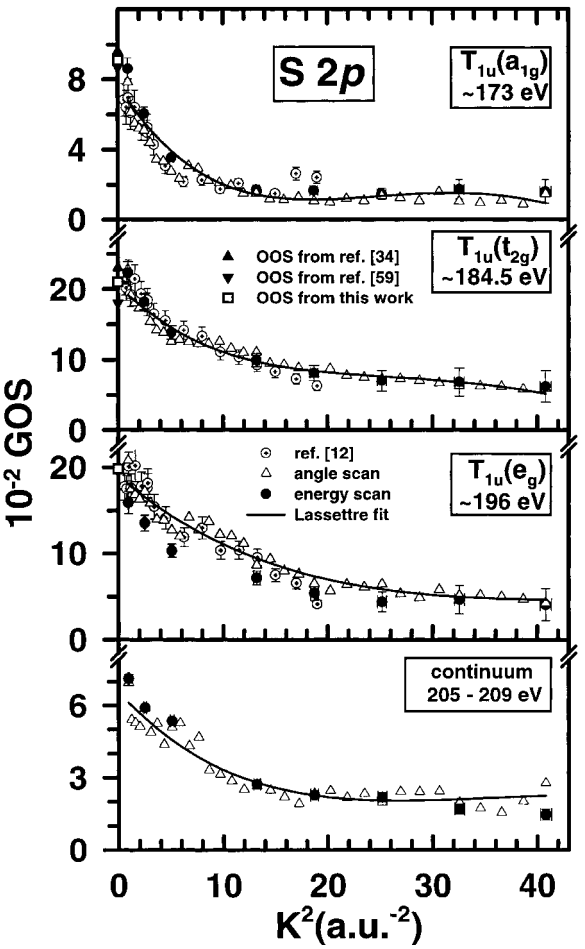

Fig. 7. GOS profiles for the $T_{1u}(a_{1g})$, $T_{1u}(t_{2g})$ and $T_{1u}(e_g)$ dipole-coupled S 2p excited states. The GOS absolute scales were established by normalization to the average literature of two OOS values for the a_{1g} and t_{2g} transitions [35,58]. The solid lines are the result of fits of the data to the Lassettre series (Eq. (6)). The optical oscillator strengths estimated from Lassettre fit extrapolation of the GOS are shown by the open squares at $K^2 = 0$.

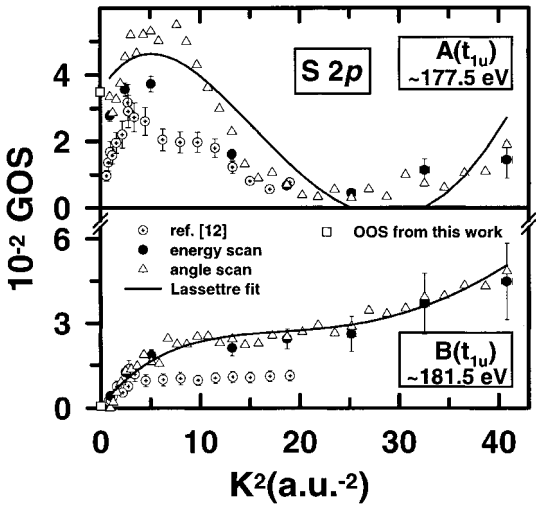

Fig. 8. GOS profiles for the $A(t_{1u})$ and $B(t_{1u})$ quadrupole-coupled S 2p excitation signals. The GOS absolute scales were set from the OOS values for the a_{1g} and t_{2g} transitions. The solid lines are the result of fits of the data to the Lassettre series (Eq. (6)). The optical oscillator strengths estimated from Lassettre fit extrapolation of the GOS are shown by the open squares at $K^2 = 0$.

and procedures we have used in this work both differ substantially from the earlier study (in particular, use of a different electron source, a different gas sample arrangement, and a different geometric correction factor). Thus, the good agreement provides strong and independent support and support that the derivation of GOS from peak areas with geometry correction is the correct approach, rather than a simple peak maximum measurement as reported by Ying et al. [1,15]. The methodology they have used ignores scattering geometry corrections and is a strong function of experimental resolution.

The GOS profile for the dipole forbidden "A state" signal shows a maximum at $K^2 \sim 4$–6 a.u.$^{-2}$, and is in good agreement with the earlier results [13]. The intensity of the A state is non-zero in the optical limit [56]. The observations suggest there are two excitation mechanisms for this state: a vibronically allowed one, which gives rise to the weak component observed optically [6,7] and a dipole-forbidden mechanism [25,56].

In the case of the $B(t_{1u})$ transition, there is good agreement between values obtained from energy-scan and angle-scan modes, and the agreement with the earlier values [13] is reasonable, at least at small K^2 values. We note that the data reported in Ref. [13] was recorded using ~0.3 eV resolution rather than the ~0.7 eV resolution of the present work. It is interesting to note that, even though the two states are associated with the same electron configuration, the excitations to the A and B states have quite different GOS profiles. The OOS for the B state is zero, and the B state GOS profile con-

Table 5
Values of the Lassettre coefficients derived from fits to the GOS profiles

	f_0 ($\times 10^{-2}$)	f_1	f_2 ($\times 10^2$)	f_3 ($\times 10^2$)	f_1/f_0	f_2/f_0 ($\times 10^3$)	f_3/f_0 ($\times 10^4$)
S 2p							
$T_{1u}(a_{1g})$	9.1	−6.4	1.6	−12.5	−60	1.8	−1.4
$A(t_{1u})$	3.5	2.5	−1.2	11	71	−3.3	3.1
$B(t_{1u})$	0.06	1.8	−0.3	2.8	2900	−57	46
$T_{1u}(t_{2g})$	21	−5.5	1.0	−6.3	−27	0.5	−0.3
$T_{1u}(e_g)$	19	−5.3	0.7	−2.8	−28	0.4	−0.2
S 2s							
$A_{1g}(a_{1g})$	1.5	−0.2	0.1	−0.7	−16	0.6	−0.5
$T_{1u}(t_{1u})$	3.6	−1.8	0.5	−3.3	−51	1.2	−0.9
$T_{2g}(t_{2g})$	0.7	0.6	−0.3	2.8	82	−3.8	3.8
$E_g(e_g)$	1.3	1.2	−0.7	7.9	88	−5.0	5.9
F 1s							
$T_{1u}(a_{1g})$	10.9	−10.1	4.1	−51	−92	3.7	−4.7
$T_{1u}(t_{1u})^a$	1.5	−1.5	0.6	−1.4	−98	3.5	−0.9
$T_{1u}(t_{1u})^b$	12.8	−11.3	4.3	−51	−89	3.9	−4.0
$T_{1u}(t_{2g})$	7.2	−7.7	3.6	−54	−108	5.0	−7.5
$T_{1u}(e_g)$	3.4	−3.7	1.9	−37	−110	5.6	−11

[a] $(2a_{1g}, 6t_{1u})T_{1u.}$
[b] $(1e_g, 6t_{1u})T_{1u.}$

tains higher signal above 10 a.u.$^{-2}$, continuing to increase right to the maximum K^2 sampled. Indeed the B state GOS is still rising at $K^2 = 113$ a.u.$^{-2}$ (13°, $E_0 = 1480$ eV) [26]. This suggests that there are at least two different states contributing to the "B state" signal, consistent with the lineshape analysis of the high resolution spectrum reported in Ref. [25].

The f_n values derived from the fit to the modified Lassettre equation (Eq. (6)) exhibit sign alternation. This was also observed by both Ying et al. [15] and Turci et al. [13]. The f_n/f_0 ratios for the dipole allowed transitions in S 2p are found to be similar in magnitude to the ones from Refs. [13,15]. The f_n/f_0 ratios determined for the A, B dipole-forbidden S 2p transitions are smaller than in the previous study [13], consistent with the observed difference in the GOS shape as well as the presence of a second maximum in both profiles, which is only seen in the present work due to the much larger K^2 range investigated.

4.2.2. S 2s

Fig. 9 presents the GOS profiles for the four S 2s transitions and for the S 2s continuum. The relative S 2s GOS were converted to an absolute scale by simultaneously measuring the S 2p $\rightarrow t_{2g}$ and S 2s $\rightarrow t_{1u}$ intensities under near-dipole conditions ($K^2 = 0.5$ a.u.$^{-2}$). The ratio of peak areas (0.205) was combined with the S 2p GOS scale factor to generate the scale factor for the S 2s GOS. Although some early results were presented elsewhere [14], the GOS for the S 2s states are mapped with high statistical accuracy for the first time and the K^2 range has been extended from a K^2_{max} of only 9 a.u.$^{-2}$ to over 40 a.u.$^{-2}$.

The GOS profile for the dipole allowed S $2s(a_{1g}) \rightarrow t_{1u}$ transition decays continuously from a maximum at $K^2 = 0$. The GOS profiles for the t_{2g} and e_g dipole forbidden transitions approach zero at $K^2 = 0$ then increase to a peak at $K^2 \sim 8$–10 a.u.$^{-2}$. Surprisingly, the GOS profile for the a_{1g} state is almost independent of K^2 and clearly extrapolates to a finite value at $K^2 = 0$, indicating there should be a detectable optical transition. It is possible that there is a vibronic mechanism active for S 2s $\rightarrow a_{1g}$ excitation in the dipole limit. The peak for the dipole-allowed S $2s(t_{1u}) \rightarrow t_{1u}$ transition in the optical (total ion yield) spectrum [25] has a shoulder on the low energy side, in the region of the a_{1g} state, consistent with the present results. S 2s transitions to dipole-forbidden states are

clearly enhanced with increasing momentum transfer. Thus, at high momentum transfer (Fig. 6), the three non-dipole transitions at 237.3 eV (A_{1g}), 246.9 eV (T_{2g}) and 258.9 eV (E_g) become relatively more intense than the dipole-allowed transition at 240.5 eV (T_{1u}). In the strong non-dipole regime, the A_{1g} transition dominates the spectrum (Fig. 6). Fig. 9 also plots fits of the GOS profiles to the modified Lassettre function. The general trend for alternating signs in the coefficients is consistent with the spectral assignments [25], which are not controversial.

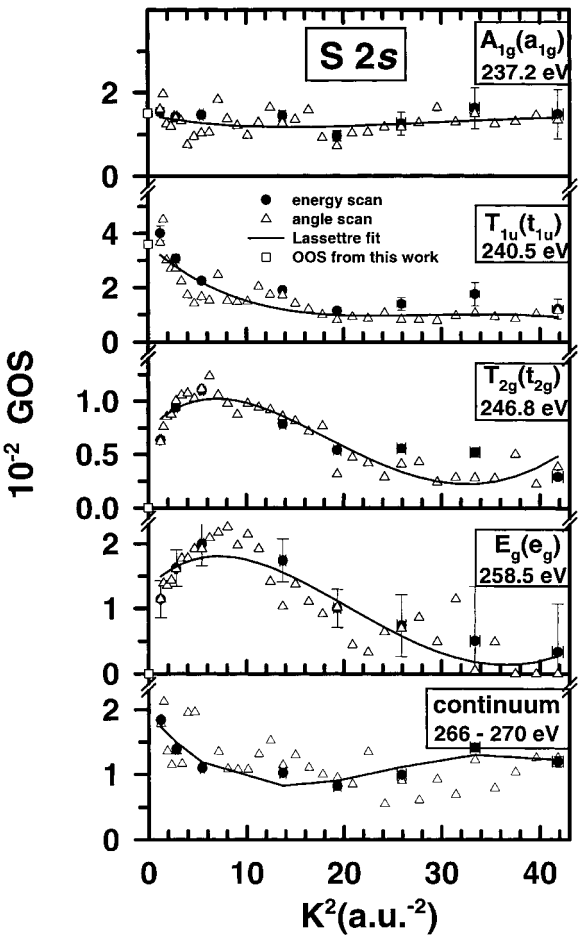

Fig. 9. GOS profiles for the $T_{1u}(t_{1u})$ dipole-coupled S 2s excited state and for the $A_{1u}(a_{1u})$, $T_{2g}(t_{2g})$ and $E_g(e_g)$ quadrupole-coupled S 2s excited states. The absolute GOS scale was set by correlating S 2s and S 2p scales in a simultaneous measurement of both edges under near-dipole conditions. The solid lines are the result of fits of the data to the Lassettre series (Eq. (6)). The optical oscillator strengths estimated from Lassettre fit extrapolation of the GOS are shown by the open squares at $K^2 = 0$.

4.2.3. F 1s

Fig. 10 presents the GOS profiles for F 1s excitations and for the F 1s continuum of SF_6. This

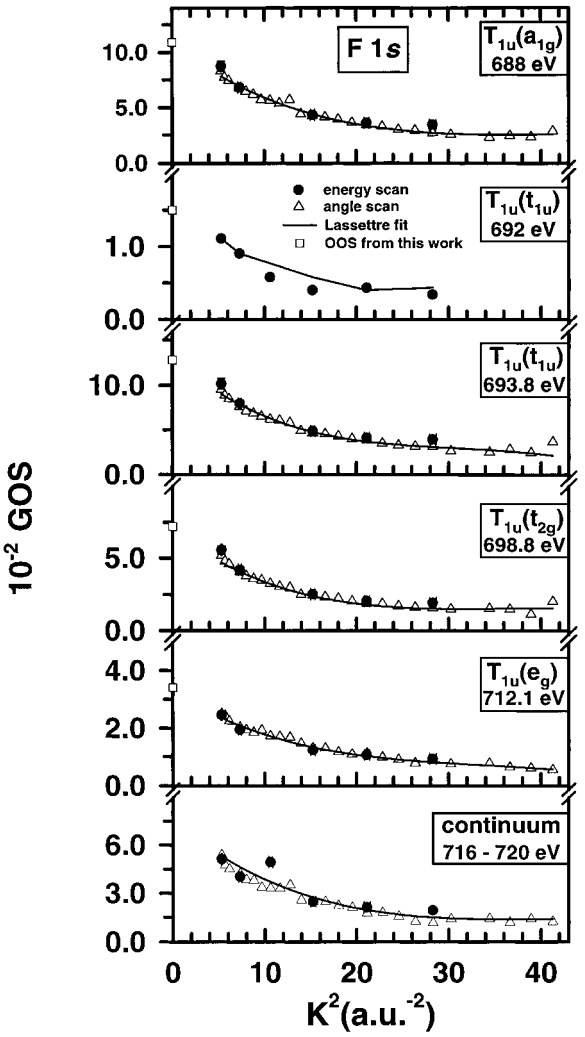

Fig. 10. GOS profiles for the $T_{1u}(a_{1g})$, $T_{1u}(t_{1u})$, $T_{1u}(t_{2g})$ and $T_{1u}(e_g)$ dipole-coupled F 1s excited states. The absolute GOS scale was set by atomic continuum normalization [59] (see text for details). The solid lines are the result of fits of the data to the Lassettre series (Eq. (6)). The optical oscillator strengths estimated from Lassettre fit extrapolation of the GOS are shown by the open squares at $K^2 = 0$.

is the first report of GOS profiles for F 1s excitation of SF_6. The relative GOS of the F 1s $\rightarrow a_{1g}$ transition was extrapolated to $K^2 = 0$ and set to 0.108 per F atom for this transition, the OOS value for the a_{1g} transition derived by atomic continuum normalization [59]. The independence of the F 1s spectral shape on K^2 means that atomic continuum normalization at finite K^2 is not a significant source of error.

The group theory analysis shows that there are five dipole accessible F 1s excited states [25]. The GOS profiles for each of the five resolvable bands $(1t_{1u},6a_{1g})T_{1u}$, $(2a_{1g},6t_{1u})T_{1u}$, $(1e_g,6t_{1u})T_{1u}$, $(1t_{1u}, 2t_{2g})T_{1u}$ and $(1t_{1u},4e_g)T_{1u}$ are consistent with a dipole-allowed character of the transitions. Dipole transitions may dominate F 1s excitation because promotions to all five virtual valence orbitals can occur from either the gerade ($2a_{1g}$, $1e_g$) or the ungerade ($1t_{1u}$) F 1s molecular orbitals, as required to fulfill dipole selection rules. Fig. 10 also plots fits of the F 1s GOS profiles to the modified Lassettre function. The signs of the coefficients derived from fitting the modified Lassettre function to the measured F 1s GOS profiles alternate (Table 4). This suggests that dipole transitions dominate at all momentum transfer, in apparent contrast to the suggestion from a theoretical study of O 1s GOS profiles of CO_2 [11] that there might be large non-dipole contributions in cases of core excitation from symmetry equivalent sites like the F 1s levels of SF_6. Theoretical studies of the GOS profiles of SF_6 would be of considerable interest to further investigate this point.

5. Summary

A high performance inelastic electron scattering spectrometer, optimized for flexible studies of inner-shell electronic excitation using variable scattering angle and variable impact energy, has been developed. The instrumentation and procedures used to obtain GOS profiles have been described. The spectrometer performance has been demonstrated by results on vibrationally resolved singlet and triplet excitations in CO and by a detailed study of the GOS profiles for creating S 2p, S 2s and F 1s excited states of SF_6 over $0.8 < K^2 < 40$ a.u.$^{-2}$. The SF_6 results confirm and greatly extend earlier work [13,25]. They support our earlier conclusion that the correct method to determine GOS values is from peak areas with proper correction for instrumental effects such as geometry-corrections, and kinematic conversion (Eq. (3)). The absolute GOS reported herein assume that the first-Born approximation is valid at the impact energies and scattering angles used. While comparison with theory is required to test this hypothesis, we do note that a recent theory–experiment comparison for the GOS for inner shell excitation of CO_2 [11] did conclude the first-Born approximation is valid over the range of experimental conditions used in this work.

Acknowledgements

This research is financially supported by NSERC (Canada). We thank the McMaster mechanical shop for their high quality work, Marek Kiela for assistance with electronics, Michel Tronc for providing drawings for the electron gun, and Fred Pearson for help with gun filaments.

References

[1] J.F. Ying, C.P. Mathers, K.T. Leung, Phys. Rev. A 101 (1994) 7311.
[2] E.N. Lassettre, A. Skerbele, Meth. Exp. Phys. 3B (1974) 868.
[3] S. Trajmar, J.K. Rice, A. Kuppermann, in: L. Prigogine, S.A. Rice (Eds.), Advanced Chemical Physics, vol. XVIII, Wiley, New York, 1970, p. 15.
[4] R.A. Bonham, in: C.R. Brundle, A.D. Baker (Eds.), Electron Spectroscopy: Theory, Techniques and Applications, vol. 3, Academic, New York, 1979, p. 127.
[5] H. Bethe, Ann. Phys. (Leipzig) 5 (1930) 325.
[6] M. Inokuti, Rev. Mod. Phys. 43 (1971) 297.
[7] R.S. Barbieri, R.A. Bonham, Phys. Rev. A 45 (1992) 7929.
[8] J.S. Lee, J. Chem. Phys. 67 (1977) 3998.
[9] A.C.A. Souza, G.G.B. de Souza, Phys. Rev. A 38 (1988) 4488.
[10] R. Camilloni, E. Fainelli, G. Petracelli, G. Stefani, J. Phys. B: Atom. Mol. Phys. 20 (1987) 1839.
[11] I.G. Eustatiu, T. Tyliszczak, A.P. Hitchcock, C.C. Turci, A.B. Rocha, C.E. Bielschowsky, Phys. Rev. A 61 (2000) 42505.

[12] H.M. Boechat Roberty, C.E. Bielschowsky, G.G.B. de Souza, Phys. Rev. A 44 (1991) 1694.
[13] C.C. Turci, J.T. Francis, T. Tyliszczak, G.G.B. de Souza, A.P. Hitchcock, Phys. Rev. A 52 (1995) 4678.
[14] A.P. Hitchcock, I.G. Eustatiu, J.T. Francis, C.C. Turci, J. Electron Spectrosc. 88–91 (1998) 77.
[15] J.F. Ying, C.P. Mathers, K.T. Leung, Phys. Rev. A. 47 (1993) R5.
[16] J.F. Ying, T.A. Daniels, C.P. Mathers, H. Zhu, K.T. Leung, J. Chem. Phys. 99 (1993) 3390.
[17] J.F. Ying, K.T. Leung, J. Chem. Phys. 100 (1994) 7120.
[18] J.F. Ying, K.T. Leung, J. Chem. Phys. 100 (1994) 1011.
[19] J.F. Ying, K.T. Leung, J. Chem. Phys. 101 (1994) 8333.
[20] J.F. Ying, C.P. Mathers, K.T. Leung, H.P. Pritchard, C. Winstead, V. McKoy, Chem. Phys. Lett. 212 (1993) 289.
[21] I. Harrison, G.C. King, J. Phys. B 19 (1986) L447.
[22] I. Harrison, G.C. King, J. Electron Spectrosc. Relat. Phenom. 43 (1987) 155.
[23] J.T. Francis, C. Enkvist, S. Lunell, A.P. Hitchcock, Can. J. Phys. 72 (1994) 879.
[24] J.T. Francis, N. Kosugi, A.P. Hitchcock, J. Chem. Phys. 101 (1994) 10429.
[25] J.T. Francis, C.C. Turci, T. Tyliszczak, G.G.B. de Souza, N. Kosugi, A.P. Hitchcock, Phys. Rev. A 52 (1995) 4665.
[26] I.G. Eustatiu, T. Tyliszczak, A.P. Hitchcock, Chem. Phys. Lett. 300 (1999) 676.
[27] E. Harting, F.H. Read, Electrostatic Lenses, Elsevier, Amsterdam, 1976.
[28] T. Mulvey, M.J. Wallington, Rep. Prog. Phys. 36 (1973) 347.
[29] J.A. Simpson, C.E. Kuyatt, J. Appl. Phys. 37 (1966) 3805.
[30] E.M. Purcell, Phys. Rev. 54 (1938) 818.
[31] F.H. Read, J. Comer, R.E. Imhof, J.N.H. Brunt, E. Harting, J. Electron Spectrosc. 4 (1974) 293.
[32] S. Daviel, C.E. Brion, A.P. Hitchcock, Rev. Sci. Instrum. 55 (1984) 182.
[33] E.N. Lassettre, J. Chem. Phys. 43 (1965) 4479.
[34] M.A. Dillon, E.N. Lassettre, J. Chem. Phys. 62 (1975) 2373.
[35] W.M. Huo, J. Chem. Phys. 71 (1979) 1593.
[36] J.L. Dehmer, J. Chem. Phys. 56 (1972) 4496.
[37] V.I. Nefedov, J. Struct. Chem. 11 (1970) 299.
[38] J.L. Dehmer, D. Dill, Phys. Rev. Lett. 35 (1975) 213.
[39] D. Dill, J. Chem. Phys. 65 (1976) 5327.
[40] J.L. Dehmer, A.C. Parr, S.H. Southworth, in: G.V. Marr (Ed.), Handbook on Synchrotron Radiation, vol. 2, North-Holland, Amsterdam, 1987 (Chapter 5).
[41] J. Stöhr, NEXAFS Spectroscopy, Springer Series in Surface Sciences, vol. 25, 1992, Springer, Heidelberg.
[42] C.E. Kuyatt, J.A. Simpson, Rev. Sci. Instrum. 38 (1967) 103.
[43] C.E. Kuyatt, Lecture Notes on Electron Optics, 1967, unpublished.
[44] D.A. Dahl, J.E. Delmore, SIMION PC/2 version 3.1 Idaho National Laboratory, EG, G Idaho Inc., Idaho Falls, ID 83415.
[45] D.W.O. Heddle, N. Papadovassilakis, J. Phys. E: Sci. Instrum. 17 (1984) 599.
[46] D.W.O. Heddle, J. Phys. E 4 (1971) 589.
[47] A.P. Hitchcock, J. Electron Spectroscopy, in press.
[48] M. Tronc, G.C. King, F.H. Read, J. Phys. B 13 (1980) 999.
[49] D.A. Shaw, G.C. King, F.H. Read, D. Cvejanovic, J. Phys. B 15 (1982) 1785.
[50] R.N.S. Sodhi, C.E. Brion, J. Electron Spectrosc. 34 (1984) 363.
[51] P. Aebi, T. Tyliszczak, A.P. Hitchcock, K.M. Baines, T.K. Sham, T.E. Jackman, J-M. Baribeau, D.J. Lockwood, Phys. Rev. B 45 (1992) 13579.
[52] R.T. Brinkmann, S. Trajmar, J. Phys. E. Sci. Instrum. 14 (1981) 245.
[53] R.A. Bonham, H.F. Wellenstein, J. Appl. Phys. 44 (1973) 2631.
[54] R.S. Barbieri, R.A. Bonham, Phys. Rev. A 44 (1991) 7361.
[55] A. Haffad, Z. Felfli, A.Z. Msezane, D. Bessis, Phys. Rev. Lett. 76 (1996) 2456.
[56] E. Hudson, D.A. Shirley, M. Domke, G. Remmers, A. Puschmann, T. Mandel, C. Xue, G. Kaindl, Phys. Rev. A 47 (1993) 316.
[57] A.P. Hitchcock, C.E. Brion, Chem. Phys. 33 (1978) 55.
[58] D. Blechschmidt, R. Haensel, E.E. Koch, U. Nielsen, T. Sagawa, Chem. Phys. Lett. 14 (1972) 33.
[59] A.P. Hitchcock, D.C. Mancini, J. Electron Spectrosc. 67 (1994) 1.
[60] W.L. Jolly, K.D. Bomben, C.J. Eyermann, At. Data Nucl. Data Tables 31 (1984) 433.
[61] R.W. Shaw Jr., T.X. Caroll, T.D. Thomas, J. Am. Chem. Soc. 95 (1973) 5870.